Key Information Retrieval in Hyperspectral Imagery through Spatial-Spectral Data Fusion

Fereidoun A. MIANJI [1], Ye ZHANG [1], Asad BABAKHANI [2]

[1]School of Electronics and Information Engineering, Harbin Institute of Technology, P.O.B. 314, Xi Da Zhi Street, Harbin-150001, Heilongjiang, China
[2] Gamma Irradiation Research Center, North Karegar Street., Tehran, Iran

fmianji@ieee.org, zhye@hit.edu.cn, a1349b@gmail.com

Abstract. *Hyperspectral (HS) imaging is measuring the radiance of materials within each pixel area at a large number of contiguous spectral wavelength bands. The key spatial information such as small targets and border lines are hard to be precisely detected from HS data due to the technological constraints. Therefore, the need for image processing techniques is an important field of research in HS remote sensing. A novel semisupervised spatial-spectral data fusion method for resolution enhancement of HS images through maximizing the spatial correlation of the endmembers (signature of pure or purest materials in the scene) using a superresolution mapping (SRM) technique is proposed in this paper. The method adopts a linear mixture model and a fully constrained least squares spectral unmixing algorithm to obtain the endmember abundances (fractional images) of HS images. Then, the extracted endmember distribution maps are fused with the spatial information using a spatial-spectral correlation maximizing model and a learning-based SRM technique to exploit the subpixel level data. The obtained results validate the reliability of the technique for key information retrieval. The proposed method is very efficient and is low in terms of computational cost which makes it favorable for real-time applications.*

Keywords

Key information retrieval, hyperspectral imagery, material radiance, spectral unmixing, superresolution.

1. Introduction

Measuring the radiance of materials within each pixel area at a very large number of contiguous spectral wavelength bands is the basis of hyperspectral (HS) imaging [1]. It provides us with both spectral and spatial information of the object. The amount of reflected, absorbed, or emitted radiation (the radiance) from materials depends on the wavelength of these radiations. The measured reflectance is called spectral signature and can be used to identify specific materials in a scene. HS imaging is of great interest in many scientific and engineering applications but the most important application for it is in remote sensing (Fig. 1). Remote sensing is a powerful tool for environmental and geological studies, civil engineering, and target detection and tracking, etc. [2].

HS images have a three dimensional (3D) data structure including two spatial and one spectral dimension. Fig. 2 shows this structure which is called "Data Cube". Each plane in a spectral band is a grayscale image depicting the spatial distribution of the reflectance of the scene in the corresponding spectral wavelength. In contrast, if we plot the spectral values in a spatial location as a function of wavelength, the result is the average spectrum of all the materials (endmembers) in the corresponding ground resolution cell.

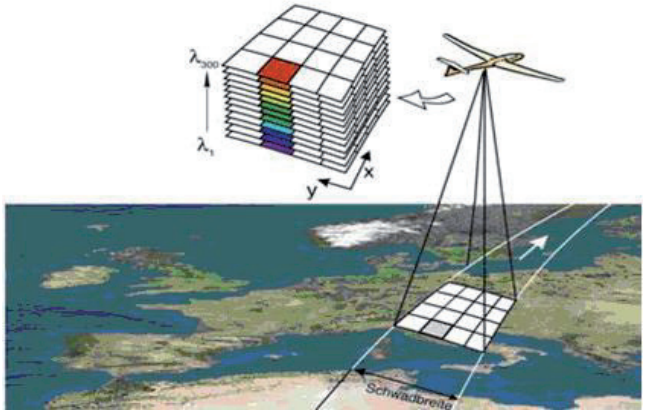

Fig.1. HS remote sensing: gathering spatial and spectral information through an airborn HS imaging sensor.

HS imaging systems are mainly designed to gather high resolution spectral information of the scene. Thus, HS images are rich in spectral information but relatively poor in spatial resolution which usually varies from few to tens of meters. In theory, any part of the electromagnetic spectrum can be recorded using HS sensors, however, technological constraints seriously limit the resolution and areas of the spectrum which can be measured at the same time. These facts make the spatial resolution one of the most expensive and hardest to improve in imaging systems [3-5] and highlight a clear need for post processing of the acquired images. To improve the spatial resolution of HS

images, we can make use of superresolution techniques together with the information at different wavelengths of the sensed object that is available with HS sensors. Many different algorithms for spatial resolution enhancement of HS images have been proposed in the last decade [6-25].

In many of the proposed methods the spatial information of a monochrome or RGB high resolution (HR) image is imposed onto the low resolution (LR) HS image [8-12]. The main limitation of all these joint processing methods is their need to a plenty of supplementary HR information. In other words, it is a multisource or multisensor method which needs an HR image of the same size of the LR HS image for resolution enhancement. Indeed, this is unapproachable in many practical problems.

Some other approaches are based on spectral mixture analysis (SMA) or subpixel classification [13-20]. These approaches estimate abundances of endmembers and provide more accurate representation of landcovers than the original HS image. SMA doesn't need supplementary source of information but it only describes mixed pixels by the abundances of endmembers without defining their spatial distribution within the pixels.

Superresolution mapping (SRM) is a different approach by which the spatial-spectral information of HS images is exploited using an HR image or a model to describe the most likely distribution of the content of mixed pixels [19-25]. Foody [19] and Nguyen et al. [21] proposed the use of a higher spatial resolution image for predicting the location of endmembers within a pixel. The main disadvantage of these algorithms is that it is difficult to obtain two coincident images of the same size and different spatial resolutions.

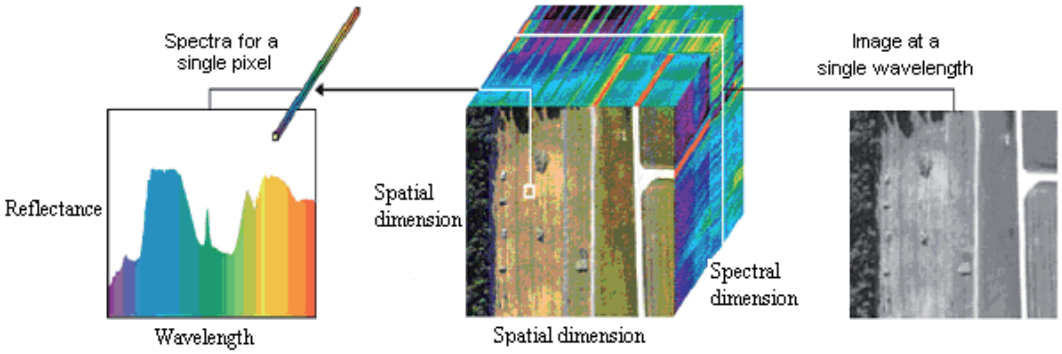

Fig. 2. A data cube (middle), the spectra for a single pixel (left) and the image at a single wavelength (right).

Autonomous approaches are independent of any HR source of data. Tatem et al. proposed a learning-based algorithm which utilizes a Hopefield neural network (HNN) for resolution enhancement without using any secondary source of data [22]. This method presents a very good efficiency but suffers a high computational cost. Gu et al. introduced a method to overcome the problem of high computational cost through a fast learning-based algorithm which integrates the spatial and spectral information of HS images [24]. Their technique exploits the spatial resolution of HS images using a learning-based SRM algorithm and some unassociated ground truth information. It is efficient in terms of computational cost, however, shows a poorer efficiency compared to the HNN method.

The aforementioned limitations, i.e., insufficient accuracy, the high computational cost and the need for huge amount of supplementary information have been the motivation for the proposed fast semisupervised resolution enhancement algorithm. To this end, we propose a learning-based algorithm for spatial resolution enhancement of HS images. Our method enhances the spatial resolution of HS images through fusing their spatial and spectral information. To benchmark the proposed method, it is compared to a very efficient unsupervised superresolution mapping technique proposed by Tatem et al. This method utilizes Hopfield neural network (HNN) and uses the same fractional images (outputs of the unmixing process) as the input [22]. It converts the subpixel mapping task into a minimum optimization model, where the spatial dependence is modeled as an energy function. Hence, a "best guess" map of the spatial distribution of the class components in each pixel is obtained through minimization of the energy function.

The reminder of this article is organized as follows. In section 2, the outline of the proposed algorithm is presented. In section 3, endmember extraction techniques in HS imagery is described. In section 4, the necessary background for spectral mixture analysis and classification of HS data is given. Section 5 provides a complete explanation about the proposed superresolution mapping (SRM) technique and in section 6 backpropagation neural network (BPNN) and the proposed training method are introduced. A quantitative assessment method for validation of the results is presented in section 7. Experiments and results are discussed in section 8 and conclusion is drawn in section 9.

2. Outline of the Proposed Technique

The proposed technique consists of four main parts, i.e., endmember extraction, spectral unmixing, training of the SRM algorithm, and superresolution mapping. The complete processing scheme is depicted in Fig. 3. The LR HS test image stands for the LR HS image from a scene

which needs to be spatially improved. The HR HS training data is a small set of HR HS samples from the same scene which are required for training of the SRM algorithm in our method. First, we define the endmembers of the LR HS test image and the HR HS training image with the help of the MNF and PPI techniques (section 3). Then, the linear spectral unmixing is applied on the test and training HS images to extract the spatial information of the endmembers. This is carried out using the developed linear mixture model (LMM) and fully constrained least squares (FCLS) algorithm which are discussed in section 4. The result of this step is the fractional images for both the test and training images. It is worth mentioning that the obtained fractional images for the test image only present the spatial distribution of the endmembers in the pixel level. The aim of the proposed method is defining the subpixel level endmember distribution information for the LR HS test image.

The third step is training of the designed SRM algorithm with the fractional images derived from the HR HS training image. It is worth noting that the HR HS training image can be the HR information of any small area of the same scene. Now our SRM algorithm has the capability to predict the subpixel level spatial information for any other area of the LR HS test image. The proposed method alleviates the problem of need to an HR image of the same size with the LR HS image. Sufficiency of a small set of HR samples in our method dramatically reduces the cost of field observation. The final step is application of the trained SRM algorithm to any desired ROI of the test image. The relationship between the abundances of the endmembers in each pixel and its neighboring pixels, learned from the HR training samples, are used in this step. We utilize the learned relationship for assigning the endmembers to the subpixels with respect to their contribution in each pixel. The basis of this LR to HR mapping by the SRM algorithm is spatial correlation maximization. Supplementary explanation about the proposed method is provided in section 5.

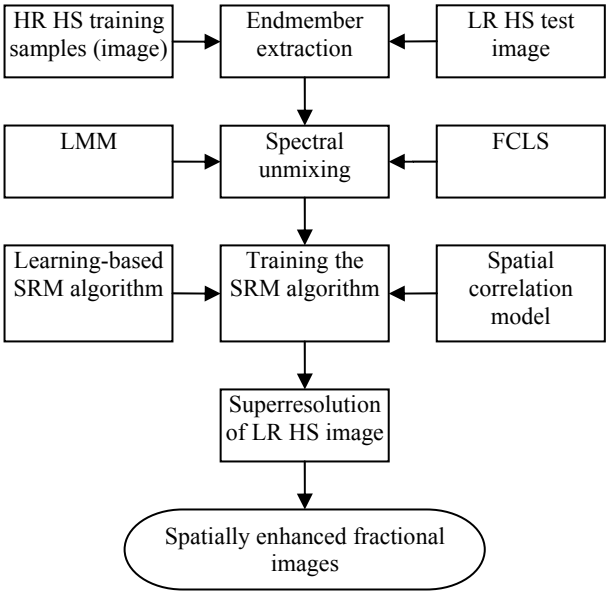

Fig. 3. Outline of the proposed technique.

3. Endmember Extraction Technique

Spectral mixture analysis has received a considerable attention over the last 15 years and a number of unsupervised/supervised algorithms for endmember extraction of HS images have been introduced. Some of the most widely used SMA techniques are N-FINDER [26], pixel purity index (PPI) [27], manual endmember selection tool (MEST) [28], convex cone analysis (CCA) [29], iterative error analysis (IEA) [30], optical real-time adaptative spectral identification system (ORASIS) [31], simulated annealing algorithm (SAA) [32], and automated morphological endmember extraction (AMEE) [33].

Presence of pure class pixels in an image depends on the sensor spatial resolution. Hence, in situations where it is not possible for a certain algorithm to find such pure pixels in a scene, the fractional components found for the mixed pixels are usually expressed in terms of other mixed pixels (the identified endmembers) and not in terms of pure classes [34, 35].

The PPI algorithm, which is used for endmember extraction in this paper, is an unsupervised technique which consists of two steps. First, a "noise-whitening" and dimensionality reduction step is performed by using the minimum noise fraction (MNF) transform [27]. Then, all the points in the resulted *N*-dimensional MNF-transformed space are projected onto many randomly generated lines and the points falling at the extremes of each line are counted. The pixels that count above a desired threshold are the purest pixels and these potential endmember spectra are loaded into an interactive *N*-dimensional visualization tool to be rotated in real time until a desired number of endmembers are visually identified as extreme pixels in the data cloud. It should be emphasized that the classification stage is a preparation step for the proposed algorithm, therefore, any other endmember extraction technique is applicable for this purpose. For instance, by adopting an automatic endmember extraction technique such as N-FINDER, the whole algorithm can be fully automated.

4. Spectral Mixture Analysis

Existence of mixed pixels in HS images, especially on the edges of the objects is a severe obstacle in high spatial resolution applications. Mixed pixels are pixels of the image which contain more than one endmember (Fig. 4).

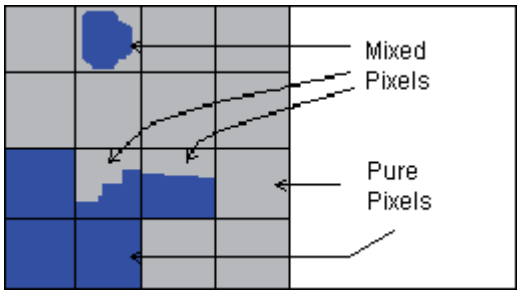

Fig. 4. Pure pixels and mixed pixels.

Despite the sources of nonlinearity in HS imaging such as bidirectional reflectance distribution function (BRDF) especially in landcover classification applications [36-37], a frequent assumption in HS remote sensing is that spectral signatures result from linear combinations of endmember spectra. These approaches largely ignore the inherent nonlinear characteristics of the hyperspectral data [38-41].

4.1 Linear Mixture Model (LMM)

Endmember spectra are endmember components in N-dimensional space. Let L equal the number of endmembers presented in an image scene with l ranging from 1 to L. Each spectrum of the scene (for every pixel) consists of N discrete wavelengths (λ_n) where n=1 to N. Let $S^l(\lambda_n)$ represent the spectral response of material l at wavelength λ_n. Each spectrum in the library is described by the following vector:

$$\mathbf{S}^l = (S^l(\lambda_1), S^l(\lambda_2), ..., S^l(\lambda_N)). \quad (1)$$

For an unknown spectra $\mathbf{u} = (u_1, u_2, \ldots, u_N)$ each vector component is composed of a linear combination of L endmembers. $\mathbf{u}$ is related to L by the estimation vector $\mathbf{x} = (x_1, x_2, \ldots, x_L)$ where

$$0 \le x_l \le 1, \quad (2)$$

$$\sum_{l=1}^{L} x_l = 1. \quad (3)$$

For a mixture described by $\mathbf{u}$, the spectral response at λ_n, $S^{\mathbf{u}}(\lambda_n)$, would be as follow:

$$S^u(\lambda_n) = \sum_l x_l S^l_{\lambda_n} \quad (4)$$

The difference between the calculated spectral response at λ_n and the actual spectral response of $\mathbf{u}$ at λ_n is

$$e_n = (u_n - \sum_l x_l S^l_{\lambda_n}) . \quad (5)$$

The goal of linear spectral unmixing is to minimize e_n. Consequently, the reflectance of a single pixel can be considered as the linear mixture of all the endmembers within a pixel [42, 43].

4.2 Unmixing

Some algorithms have been developed to handle the LMM according both the nonnegativity and sum-to-one constraints respectively represented by (2) and (3). These algorithms tend to be computationally intensive as the number of endmembers increases. Among them, the FCLS algorithm can efficiently meet both abundance constraints and is optimal in terms of least squares error [44]. The main problem of FCLS in concrete processing is that, unlike the sum-to-one constraint which can be solved by a closed-form solution, it does not have a closed-form mathematical solution for the nonnegativity constraint since it is formed by a set of L linear inequalities rather than equalities; thus, a numerical solution is always required.

In general, a nonnegatively constrained least squares problem can be described by the following optimization problem:

$$\text{Minimize} \quad LSE = (\mathbf{Sa} - \mathbf{r})^T (\mathbf{Sa} - \mathbf{r}) \quad (6)$$
$$\text{Subject to } a_j \ge 0$$

where the LSE is used as the criterion for optimality and $a_j \ge 0$, $1 \le j \le L$ represents the nonnegativity constraint. $\mathbf{S}$ is the $N \times L$ endmember matrix denoted by $[\mathbf{s}_1, \mathbf{s}_2, ..., \mathbf{s}_L]$, where $\mathbf{s}_j$ is the $l \times 1$ column vector represented by the jth endmember resident in the image scene, and $\mathbf{r}$ is an $l \times 1$ column pixel vector (of the image scene). The solution for these inequalities is possible through a Lagrangian J as follows:

$$J = \frac{1}{2}(\mathbf{Sa} - \mathbf{r})^T (\mathbf{Sa} - \mathbf{r}) + \lambda(\mathbf{a} - \mathbf{c}) \quad (7)$$

where $\lambda = (\lambda_1, \lambda_2, \ldots, \lambda_L)^T$ is the Lagrange multiplier vector, and $\mathbf{c} = (c_1 + c_2 + ..., c_L)$ is an unknown L-dimensional positive constraint vector with $c_j > 0$ for $1 \le j \le L$ to take care of the nonnegativity constraint. With $\mathbf{a} = \mathbf{c}$ and

$$\left.\frac{\partial J}{\partial \mathbf{a}}\right|_{\mathbf{a}} = 0 \Rightarrow \mathbf{S}^T\mathbf{S}_{\mathbf{a}} - \mathbf{S}^T\mathbf{r} + \lambda = 0 \quad (8)$$

the following two iterative equations are resulted

$$\hat{\mathbf{a}} = (\mathbf{S}^T\mathbf{S})^{-1}\mathbf{S}^T\mathbf{r} - (\mathbf{S}^T\mathbf{S})^{-1}\lambda, \quad (9)$$

$$\lambda = \mathbf{S}^T(\mathbf{r} - \mathbf{S}_{\hat{\mathbf{a}}}). \quad (10)$$

In order to satisfy the sum-to-one constraint, a new signature matrix $\mathbf{S'}$, is defined by including the constraint in the signature matrix $\mathbf{S}$.

$$\mathbf{S}' = \begin{bmatrix} \delta\mathbf{S} \\ 1^T \end{bmatrix} \quad (11)$$

with $1 = (1, 1, ..., 1)^T$ and a vector $\mathbf{r}'$ by

$$\mathbf{r}' = \begin{bmatrix} \delta\mathbf{r} \\ 1 \end{bmatrix}. \quad (12)$$

where δ is a constant to control the impact of the abundance sum-to-one constraint and has a typical value of 1×10^{-5} [45].

5. Superresolution Mapping (SRM) Algorithm

Superresolution mapping is estimating the spatial dependence of the components within the pixels of an image. Here, the SRM aims at predicting the location of endmembers within a mixed pixel according to the proportions defined by the SMA to improve the spatial resolution of the resulting landcover maps (fractional images).

The basis for the proposed SRM technique is spatial correlation of the endmembers. It means that the endmembers within a pixel tend to be assigned to the subpixels with a higher contribution of the same endmember in the subpixel's neighboring area. This idea is explained in Fig. 5. Fig. 5(a) shows the contribution of endmember A in a 3 × 3 window of a hypothetical fractional image obtained through a linear spectral unmixing process. The aim is defining the best subpixel level endmember assignment for the middle pixel. Fig. 5(b), for example, shows a possible random assignment in which the spatial correlation of endmember A is not taken into account. In contrast, Fig. 5(c) depicts a much better mapping and the assigned subpixels are the best in terms of spatial correlation of endmember A.

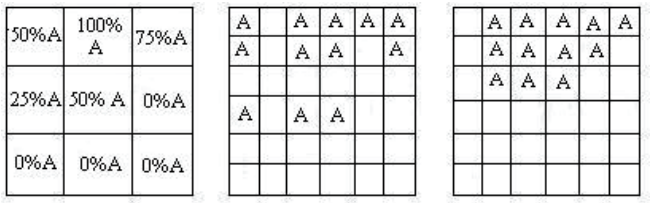

Fig. 5. The basis for the proposed SRM technique.

In order to define the location of the endmembers within a pixel of an HS image we only consider the first layer of the neighboring pixels in our model. In other words, the used SRM kernel is a 3 × 3 window as Fig. 6. Hence, the SRM model would be described in the mathematical form as (13). $f^k_{i,j}$ is a pixel of the k_{th} original LR fractional image and $f^k_{i,j}\ (q)|_{q=1,2,3,4}$ are its subpixels. The SRM function in (13) follows a binary decision rule by which the value of each subpixel is defined according to its belonging to the target class. This is explained by (14).

$$\begin{bmatrix} f^k_{i-1,j-1} & f^k_{i-1,j} & f^k_{i-1,j+1} \\ f^k_{i,j-1} & f^k_{i,j} & f^k_{i,j+1} \\ f^k_{i+1,j-1} & f^k_{i+1,j} & f^k_{i+1,j+1} \end{bmatrix}$$

Fig. 6. The 3 × 3 kernel of SRM model.

$$\begin{bmatrix} f^k_{i,j}(1) & f^k_{i,j}(2) \\ f^k_{i,j}(3) & f^k_{i,j}(4) \end{bmatrix} = SRM(f^k_{i,j}) \tag{13}$$

where

$$f^k_{i,j}(q) = \begin{cases} 1, \text{ if the subpixel of } f_{i,j} \text{ is assigned to the target class} \\ 0, \text{ otherwise} \end{cases} \tag{14}$$

This model utilizes the assumption of tendency of spatially proximate observations to be more alike than distant ones [21, 24, 46]. The necessary spatial distribution rule can be extracted through an appropriate learning-based network designed as our SRM algorithm. According to the explained procedure in Fig. 3, a small set of HR HS samples from the same scene is needed for training of the learning-based SRM algorithm. These training samples can be obtained through a proper method such as field observation or high resolution images. First, we unmix these HR HS training samples to obtain the HR fractional training samples. Then, we subsample the HR fractional training samples to obtain the LR fractional training samples. These LR fractional training samples are of the same resolution with the LR test image. Thus, if we train the SRM algorithm with the LR and HR fractional training samples as the input and target vectors, respectively, it would be capable to efficiently enhance the resolution of the LR test image.

Based on the SRM model in (13), we define the sum of square error (SSE) E as follows [24]:

$$E = \frac{1}{2}\sum \|T_z - O_z\|^2 \tag{15}$$

where T_z is the target output pattern vector denoted by $t^l_{i,j}(q)$, q = (1, 2, 3, 4) and O_z is the output pattern vector of the network denoted by $f^l_{i,j}(q)$, q = (1, 2, 3, 4). To minimize E and obtain the optimal SRM, an effective learning algorithm consisting of a backpropagation neural network (BPNN) is adapted in this work.

6. Backpropagation Neural Network (BPNN)

Backpropagation neural network was created by generalizing the Widrow-Hoff learning rule to multiple-layer networks and nonlinear differentiable transfer functions [47]. BPNNs is one of the most widely used techniques in resolution enhancement. The learning algorithm focuses on determining the connection weights between the nodes of neighbor layers. After sufficient learning, a new input typically leads to an output similar to the correct output for input vectors used in training that are similar to the new input being presented. This generalization property makes it possible to train a network on a representative set of input/target pairs and get good results without training the network on all possible input/output pairs. BPNNs often have one or more hidden layers of nonlinear neurons followed by an output layer of linear neurons. This architecture allows the network to learn nonlinear and linear relationships between input and output vectors.

Fig. 7 shows a typical 3 layer BPNN in which x_i, y_j, and $\boldsymbol{O}_q$ are the inputs, outputs from the hidden layer nodes, and outputs from the output layer nodes, respectively. v_{ij} and w_{jq} are the connection weights between the nodes of layers. Two other important parameters (not shown in Fig. 7) are bh_j and bo_q which are the bias values for the hidden and output layers, respectively. All neurons are fully connected and the functions for the output layer nodes are as follows:

$$o_q = g(\sum_{j=1}^{h} w_{jq} y_j - bo_q), \quad q = 1,\ldots,z \tag{16}$$

where $g(.)$ is the nonlinear activation function, commonly

defined as the unipolar sigmoid function

$$g(x) = \frac{1}{1+e^{-x}}. \tag{17}$$

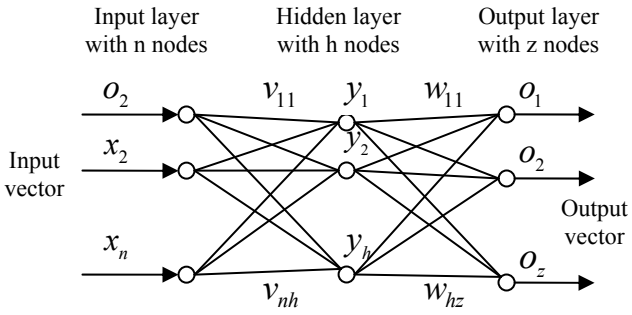

Fig. 7. A three layer BPNN.

There are four important parameters in adopting a proper BPNN architecture, namely the type of BPNN, number of hidden layers, number of nodes in each hidden layer, and the learning rate. In order to improve the performance of the standard BPNN and to avoid its two main drawbacks, i.e., slow convergence and vulnerability to local minima, a backpropagation learning algorithm with a Fletcher-Reeves version of conjugate gradient is adapted here. The general iterative algorithm of the adapted BPNN for updating the weights and bias values is

$$x_{i+1} = x_i - \alpha_i G_i \tag{18}$$

where $\boldsymbol{x}_i$ is the vector of current weights and biases, $\boldsymbol{G}_i$ is the current gradient, and α_i is the learning rate. Conjugate gradient algorithm starts by searching the steepest descent direction on the first iteration, i.e., $P_0 = -G_0$. A line search is then performed to determine the optimal distance to move along the current search direction and the next search direction is determined so that it is conjugate to the previous search direction. The general procedure is:

$$P_i = -G_i + \beta_i P_{i-1} \tag{19}$$

where for the Fletcher-Reeves

$$\beta_i = \frac{G_i^T G_i}{G_{i-1}^T G_{i-1}}. \tag{20}$$

The iteration in training stage is repeated until either the error criteria (E) or the iteration number (S) is satisfied.

Number of the neurons in the input and output layers of the network are constrained by the problem. Hence for an SRM algorithm according to (13) which considers the center pixel and its 8 neighbors as the input and with the zoom factor of 2 (zf=2), the number of neurons in the input and output layers would be 9 and 4, respectively. It is shown that one hidden layer is generally sufficient even for complex cases provided that enough nodes are available [48, 49]. Hence, with the number of hidden layers set to one, and considering the E (SSE) in the training process as the evaluation rule, necessary experiments were carried out to find the optimum values for the parameters of the network. We set the conditions of stopping the training process, namely the expected E and max iteration number (epochs) to 10^{-3} and 400, respectively. The optimum number of neurons in the hidden layer was set to 25 and the learning rate was set to 0.1.

7. Quantitative Assessment

A quantitative assessment system is necessary to evaluate the performance of the proposed method in enhancing the resolution of the LR HS images. Furthermore, it is needed to provide a standard basis for comparing the proposed technique with the HNN method. Consequently, two measures were adopted for assessing the effectiveness of the proposed method, namely, root mean square error (RMSE) and correlation coefficient (CC). RMSE and CC inform about the accuracy of the prediction (bias and variance) and the amount of association between a target and estimated set of proportions, respectively. In sum, they are two important measures of coherence between the result and the target. The definitions of *RMSE* and *CC* are given in (21) and (22).

$$RMSE = \sqrt{\frac{\sum_{i=1}^{N_1}\sum_{j=1}^{M_1}\left[(I_1)_{ij} - (I_2)_{ij}\right]^2}{N_1 M_1}}, \tag{21}$$

$$CC = \left| \frac{\sum_{i=1}^{N_1}\sum_{j=1}^{M_1}(I_1)_{i,j}(I_2)_{i,j} - N_1 M_1 \bar{I}_1 \bar{I}_2}{\sqrt{\left(\sum_{i=1}^{N_1}\sum_{j=1}^{M_1}\left[(I_1)_{ij}\right]^2 - N_1 M_1 \bar{I}_1^2\right)\left(\sum_{i=1}^{N_1}\sum_{j=1}^{M_1}\left[(I_2)_{ij}\right]^2 - N_1 M_1 \bar{I}_2^2\right)}} \right| \tag{22}$$

where I_1 and I_2 are the enhanced image with size $N_1 \times M_1$ and the original HR image with size $N_2 \times M_2$, respectively. $(I_1)_{ij}$ and $(I_2)_{ij}$ are the pixels at image coordinate (i,j) from the two images, and $\bar{I}_1$ and $\bar{I}_2$ are the means of two images. In these experiments $N_1 = N_2$, , and $M_1 = M_2$.

8. Experiments and Results

In order to validate the proposed technique two remotely sensed HS data collected by the Airborne Visible/Infrared Imaging spectrometer (AVIRIS) are chosen for the experiments. One of them is a real HS image with available ground truth map, namely HS-I. HS-I is the test image with necessary *a priori* information of the land-covers to verify the performance of the proposed SRM technique on real world HS images without the possible influence of the endmember extraction and unmixing processes. The other real world HS image without available hard classification map is HS-II. Experiment on HS-II measures the performance of the whole algorithm.

AVIRIS is a sophisticated and complex optical sensor system involving a number of major subsystems, components, and characteristics. The AVIRIS sensor receives white light in the foreoptics, disperses the light into the spectrum, converts the photons to electrons, amplifies the

signal, digitizes the signal and records the data to high density tape. The full detail of this spectrometer is available in reference [50].

8.1 Experiments on HS-I

HS-I is a remotely sensed HS image which is denoted by Indian Pines data. It was subjected to removal of the water absorption regions, low SNR, and bad bands. After these corrections, 200 available bands from the original data remained in the 0.4–2.5 μm wavelength range. Bit per pixel (bpp) for each spectral channel of this image is 16. A hard classification map (ground truth map) including 16 land cover classes (endmembers) is available for this data. Figs. 8 (a) and (b) show the hard classification map and the 25th band of the original HS-I, respectively. Fig. 9 shows the map of two of the land covers, i.e., grass/trees and woods.

(a)

(b)

Fig. 8. HS-I. (a) The hard classification map (ground truth). (b) 25th band of HS-I.

After subsampling of every land cover class with a 2 × 2 mean filter, 2500 training samples from 8 randomly selected LR land covers were input to the SRM algorithm to train it. Then, the trained SRM were applied to all of the LR land covers to enhance them. The obtained results for all of the land cover classes were very promising. The original HR, subsampled, and enhanced images for two of the land covers, namely, grass/trees and woods are shown for visual evaluation in Fig. 9. Original images were used as the standard HR images for verification of the performance of the technique and Tab. 1 shows the related RMSE and CC for these two land cover classes. To give a reference for quantitative comparison, the HNN method was also applied on the same LR land covers of HS-I. RMSE and CC of the enhanced fractional images for grass/trees and woods, obtained with HNN, are given in Tab. 2. As can be seen, RMSE of both the enhanced land-covers obtained by the proposed method is considerably better than (about half) the HNN technique. In other words, the error between the original HR images and the enhanced images using the proposed technique are less than HNN.

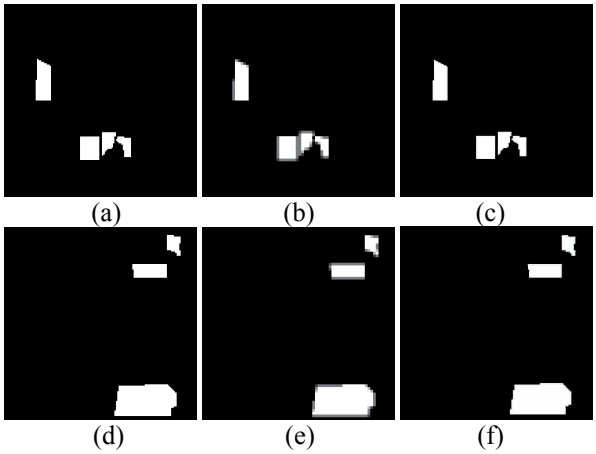

Fig. 9. Experimental results on HS-I. (a), (b), and (c) the original, subsampled, and enhanced image for grass/trees, respectively. (d), (e), and (f) the original, subsampled, and enhanced image for woods, respectively.

	Grass/trees	woods
RMSE	0.0275	0.0202
CC	0.9897	0.9968

Tab. 1. RMSE and CC values for the proposed technique with HS-I.

	Grass/trees	woods
RMSE	0.0457	0.0381
CC	0.9804	0.9941

Tab. 2. RMSE and CC values for the HNN method with HS-I.

To optimize the developed HNN program for this problem, necessary experiments were carried out on different samples in order to find the optimum parameters and for a zoom factor of 2, the size of the input window to the energy function and the iteration number were set to 3×3 (center pixel and its 8 neighbors) and 3000, respectively.

8.2 Experiments on HS-II

As the second test data, another AVIRIS data was chosen. After removal of the water absorption regions, low SNR, and bad bands, 126 available bands from the original data remained in the 0.4–1.8 μm wavelength range and the corrected HS data is denoted by San Diego data. bpp for each spectral channel of this image is 40. Fig. 10 shows the tenth band of San Diego. For experiments, an area of 100 × 100 pixel was chosen as the region of interest (ROI).

Figs. 11(a) and (b) show the tenth band of the original ROI, i.e., HS-II and the tenth band of the subsampled (with the 2×2 mean filter) HS-II, respectively. For training of the SRM algorithm, another part of San Diego which is an 80×80 pixel area, namely Train-data was chosen. Figs. 12(a), (b), and (c) show the tenth band of Train-data, subsampled Train-data (with the 2×2 mean filter), and one of the fractional images of Train-data (for asphalt), respectively.

Fig. 10. Band 10 of AVIRIS San Diego HS image.

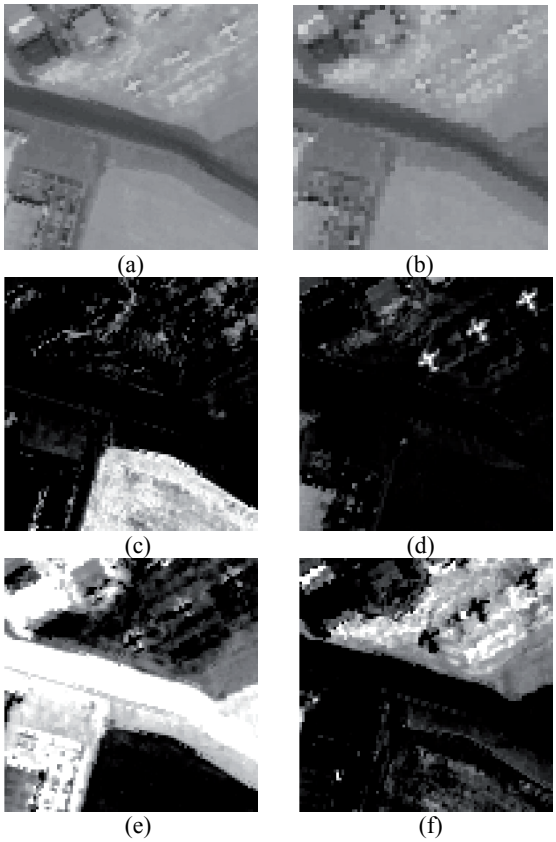

Fig. 11. HS-II. (a) Tenth band of the original HS-II. (b) Tenth band of the subsampled HS-II. (c), (d), (e), and (f) HR fractional images derived from the original HS-II.

In this stage, validation of the complete algorithm was carried out, i.e., the linear spectral unmixing and SRM techniques were tested together using the HS-II. First, with the help of MNF and PPI, four endmembers corresponding to sand (Fig. 11(c)), airplane (Fig. 11(d)), asphalt (Fig. 11(e)), and concrete (Fig. 11(f)) were extracted from HS-II. These endmembers were required for spectral unmixing of HS-II through the LMM and FCLS algorithm. Then, all necessary bands of HS-II were subsampled with the 2×2 mean filter to be fed to the linear spectral unmixing program. The outputs of this process were the LR fractional images. On the other hand, the original HS-II was directly input to the linear spectral unmixing process to yield the HR abundances (fractional images) as the standard original images for validation of the algorithm.

For training of the SRM algorithm, same process was carried out for Train-data to extract the endmembers and unmix it. The resulted fractional images were subsampled with the 2×2 mean filter to obtain the LR training fractional images. The LR fractional images and the original fractional images of Train-data were used to train the SRM algorithm as the input and target vectors, respectively. After training of the BPNN-based SRM algorithm, LR fractional images of HS-II were input to the SRM algorithm and the spatially enhanced results were compared to the standard images visually as well as quantitatively.

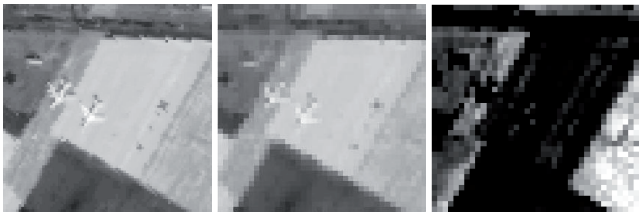

Fig. 12. Train-data. (a) Tenth band of the original Train-data. (b) Tenth band of the subsampled Train-data. (c) One of the fractional images of Train-data (for asphalt) derived from the LR (subsampled) Train-data.

Fig.13 shows the enhanced fractional images using the proposed technique in addition to the LR images. Enhancement in the resolution of the images especially on the edges is clear. RMSE and CC of the enhanced fractional images using the proposed technique is shown in Tab. 3.

	Concrete	Sand	Asphalt	Airplane
RMSE	0.0861	0.0729	0.0786	0.0511
CC	0.9650	0.9733	0.9813	0.9106

Tab. 3. RMSE and CC values for the proposed technique with HS-II.

	Concrete	Sand	Asphalt	Airplane
RMSE	0.1034	0.0756	0.0981	0.0604
CC	0.9529	0.9716	0.9708	0.8970

Tab. 4. RMSE and CC values for the HNN method with HS-II.

Tab. 4 shows the RMSE and CC for the HNN method. The results show that the error between the enhanced images and the original HR images with the proposed technique are lower compared to the HNN method, i.e., RMSE for all of the classes are decreased. In addition, the CC values using the proposed technique are superior to the CC values

obtained by HNN. But, the main advantage of the proposed method is its low computational complexity. After the initial training which takes about 15 seconds, it needs only few seconds for resolution enhancement of the test LR images, whereas the HNN method needs about 40 minutes for the same task.

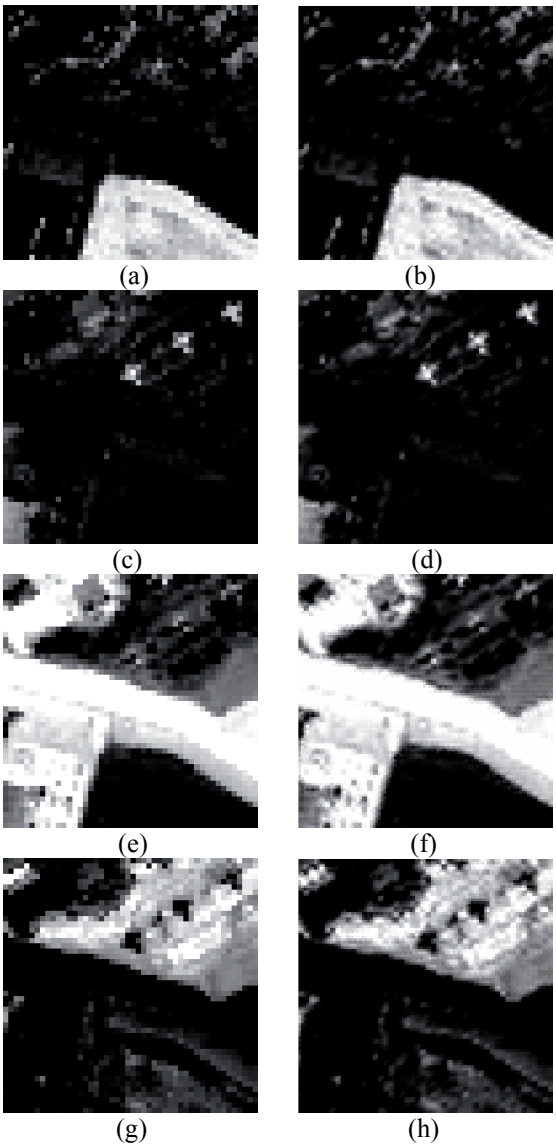

Fig. 13. Experimental results on HS-II. (a), (c), (e), and (g) the LR fractional images for sand, airplane, asphalt, and concrete, respectively. (b), (d), (f), and (h) the enhanced fractional images for sand, airplane, asphalt, and concrete, respectively.

9. Conclusion

We proposed a novel semisupervised technique for key information retrieval in hyperspectral imagery through resolution enhancement. The technique combines the SMA and a learning-based SRM algorithm for spatial-spectral data integration to exploit the subpixel detail of remotely sensed HS images. The necessary experiments were carried out on real HS images with and without available hard classification maps and the obtained results were evaluated qualitatively and quantitatively. Furthermore, as a basis for comparison, a very efficient unsupervised method, namely HNN was applied on the same test data sets. The experiments validated the effectiveness of the method and the measurements confirmed its good performance. The proposed method needs very limited HR training samples. This dramatically alleviates the shortcoming of joint processing techniques for which same size panchromatic images from the same scene are needed. It is very efficient for resolution enhancement and highly superior to the HNN method in terms of computational complexity. It is a good choice for real time target detection and tracking applications.

Acknowledgements

This work was supported by the Natural Science Foundation of China under the grants 60972143 and 60972144, and research fund for the doctorial program of higher education of China under the grant 20092302110033.

References

[1] MANOLAKIS, D., MARDEN, D., SHAW, D. A. Hyperspectral image processing for automatic target detection applications. *Lincoln Laboratory Journal*, 2003, vol. 14, no.1, p. 79-116.

[2] BUTTINGSRUD, B., ALSBERG, B. K. Superresolution of hyperspectral images. *Chemometrics and Intelligent Laboratory Systems*, 2006.

[3] MIANJI, F. A., ZHANG, Y., SULEHRIA, H. K., BABAKHANI, A., KARDAN, M. R. Superresolution challenges in hyperspectral imagery. *Information Technology Journal*, 2008, vol. 7, no. 7, p. 1030-1036.

[4] MIANJI, F. A., ZHANG, Y., BABAKHANI, A. Optimum method selection for resolution enhancement of hyperspectral imagery. *Information Technology Journal*, 2009, vol. 8, no. 3, p. 263-274.

[5] JANE, O., ILK, G. A quantitative study on optimum parameters selection in adaptive unsharp masking technique for infrared images. *Radioengineering*, 2009, vol. 18, no. 4, p. 611-617.

[6] AKGUN, T., ALTUNBASAK, Y., MERSEREAU, R. M. Super-resolution reconstruction of hyperspectral images. *IEEE Trans. Image Process*., 2005, vol. 14, no. 11, p. 1860-1875.

[7] MARIA, M. T., NUNEZ, J. Super-resolution of remotely sensed images with variable-pixel linear reconstruction. *IEEE Trans. Geosci. Remote Sens.*, 2007, vol. 45, no. 5, p. 1446–1457.

[8] HARDIE, R. C., EISMANN, M. T. MAP estimation for hyperspectral image resolution enhancement using an auxiliary sensor. *IEEE Trans. Image. Process.*, 2004, vol. 13, no. 9, p. 1174–1184.

[9] ROBINSON, G. D., GROSS, H. N., SCHOTT, J. R. Evaluation of two applications of spectral mixing models to image fusion. *Remote Sensing of Environment*, 2000, vol. 71, no. 3, p. 272–281.

[10] EISMANN, M. T., HARDIE, R. C. Hyperspectral resolution enhancement using high-resolution multispectral imagery with arbitrary response functions. *IEEE Trans. Geosci. Remote. Sens.*, 2005, vol. 43, no. 3, p. 455–465.

[11] GROSS, H. N., SCHOTT, J. R. Application of spectral mixture analysis and image fusion techniques for image sharpening. *Remote Sensing of Environment*, 1998, vol. 63, no. 2, p. 85–94.

[12] EISMANN, M. T., HARDIE, R. C. Application of the stochastic mixing model to hyperspectral resolution enhancement. *IEEE Trans. Geosci. Remote. Sens.*, 2004, vol. 42, no.9, p. 1924–1933.

[13] ATKINSON, P. M., CULTER, M. E. J., LEWIS, H. Mapping sub-pixel proportional land cover with AVHRR imagery, *Int. J. Remote Sens.*, 1997, vol. 18, no. 4, p. 917–935.

[14] WINTER, M. E., WINTER, E. M. Physics-based resolution enhancement of hyperspectral data. In *Proceedings of SPIE*, 2002, no. 4725, p. 580–587.

[15] CHEN, F., Using spectral-shape parameters to improve linear spectral mixture analysis. *Int. J. Remote Sens.*, 2009, vol. 30, no. 22, p. 6061-6067.

[16] BROWN, M., GUNN, S. R., LEWIS, H. G. Support vector machines for optimal classification and spectral unmixing. *Ecol. Model.*, 1999, vol. 120, no. 2, p. 167–179.

[17] FORERO, S. V., MANIAN, V. Improving hyperspectral image classification using spatial preprocessing. *IEEE Geosci. Remote Sens. Lett.*, 2009, vol. 6, no. 2, p. 297-301.

[18] TARABALKA, Y., BENEDIKTSSON, J. A., CHANUSSOT, J. Spectral-spatial classification of hyperspectral imagery based on partitional clustering techniques. *IEEE Trans. Geosci. Remote Sens.*, 2009, vol. 47, no. 8, p. 2973-2987.

[19] FOODY, G. M. Sharpening fuzzy classification output to refine the representation of sub-pixel land cover distribution. *Int. J. Remote Sens.*, 1998, vol. 19, no. 13, p. 2593–2599.

[20] DOBIGEON, N., TOURNERET, J. Y., CHANG, C. I. Semi-supervised linear spectral unmixing using a hierarchical Bayesian model for hyperspectral imagery. *IEEE Trans. Remote Sens. Geosci.*, Jul. 2008, vol. 56, no. 7, p. 2684-2695.

[21] NGUYEN, M. Q., ATKINSON, P. M., LEWIS, H. G. Superresolution mapping using a Hopfield neural network with fused images. *IEEE Trans. Geosci. Remote Sens.*, 2006, vol. 44, no. 3, p. 736–749.

[22] TATEM, A. J., LEWIS, H. G., ATKINSON, P. M., NIXON, M. S. Superresolution target identification from remotely sensed images using a Hopfield neural network. *IEEE Trans. Geosci. Remote Sens.*, 2001, vol. 39, no. 4, p. 781–796.

[23] MERTENS, K. C., VERBEKE, L. P. C., WESTRA, T., DE WULF, R. R. Subpixel mapping and subpixel sharpening using neural network predicted wavelet coefficients. *Remote Sens. Environ.*, 2004, vol. 91, no. 2, p. 225–236.

[24] GU, Y., ZHANG, Y., ZHANG, J. Integration of spatial-spectral information for resolution enhancement in hyperspectral images. *IEEE Trans. Geosci. Remote Sens.*, 2008, vol. 46, no. 5, p. 1347-1358.

[25] GE, Y., LI, S., LAKHAN, V. C. Development and testing of a subpixel mapping algorithm. *IEEE Trans. Signal Process.* 2009, vol. 47, no. 7, p. 2155-2164.

[26] WINTER, M. E. N-Finder: An algorithm for fast autonomous spectral end-member determination in hyperspectral data. In *Proceedings of SPIE*, 1999, vol. 3753, p. 266–275.

[27] BOARDMAN, J. W., KRUSE, F. A., GREEN, R. O. Mapping target signatures via partial unmixing of AVIRIS data. In *Summaries of the VI JPL Airborne Earth Science Workshop.* Pasadena (CA), 1995.

[28] BATESON, C. A., CURTISS, B. A method for manual endmember selection and spectral unmixing. *Remote Sens. Environ.*, 1996, vol. 55, p. 229–243.

[29] IFARRAGUERRI, A., CHANG, C.-I. Multispectral and hyperspectral image analysis with convex cones. *IEEE Trans. Geosci. Remote Sens.*, 1999, vol. 37, p. 756–770.

[30] NEVILLE, R. A., STAENZ, K., SZEREDI, T., LEFEBVRE, J., HAUFF, P. Automatic endmember extraction from hyperspectral data for mineral exploration. In *Proceedings of the 21st Can. Symp. Remote Sensing*, Ottawa, ON, Canada, 1999.

[31] BOWELS, J., PALMADESSO, P. J., ANTONIADES, J. A., BAUMBACK, M. M., RICKARD, L. J. Use of filter vectors in hyperspectral data analysis. In *Proceedings SPIE,* 1995, vol. 2553, p. 148–157.

[32] BATESON, C. A., ASNER, G. P., WESSMAN, C. A. Endmember bundles: A new approach to incorporating endmember variability into spectral mixture analysis. *IEEE Trans. Geosci. Remote Sens.*, 2000, vol. 38, p. 1083–1094.

[33] PLAZA, A., MARTINEZ, P., PEREZ, R., PLAZA, J. Spatial/spectral endmember extraction by multidimensional morphological operations. *IEEE Trans. Geosci. Remote Sens.*, 2002, vol. 40, no. 9, p. 2025–2041.

[34] PLAZA, A., MARTINEZ, P., PEREZ, R., PLAZA, J. A Quantitative and comparative analysis of endmember extraction algorithms from hyperspectral data. *IEEE Trans. Geosci. Remote Sens.*, 2004, vol. 42, no. 3, p. 650-663.

[35] WANG, J., CHANG, C.-I. Applications of independent component analysis in endmember extraction and abundance quantification for hyperspectral imagery. *IEEE Trans. Geosci. Remote Sens.*, 2006, vol. 44, no. 9, p. 2601–2616.

[36] GOORDIN, D. G., GAO, J., HENERBRY, G. M. The effect of solar illumination angle and sensor view angle on observed patterns of spatial structure in tall grass prairie. *IEEE Trans. Geosci. Remote Sens.*, 2004, vol. 42, no. 1, p. 154-165.

[37] SANDMEIER, S. R., MIDDLETON, E. M., DEERING, D. W., QIN, W. The potential of hyperspectral bidirectional reflectance distribution function data for grass canopy characterization. *Journal of Geophysical Research*, 1999, vol. 104, no. D8, p. 9547–9560.

[38] BOLTON, J., GADER, P. Random set framework for context-based classification with hyperspectral imagery. *IEEE Trans. Geosci. Remote Sens.*, Nov. 2009, vol. 47, no. 11, pp. 3810–3821.

[39] DAS, S. K., SINGH, R. Performance of kriging-based soft classification on wiFS-IRS-1D image using ground hyperspectral signatures. *IEEE Geosci. Remote Sens. Lett.*, Jul. 2009, vol. 6, no. 3, pp. 453–457.

[40] PENN, B. S. Using simulated annealing to obtain optimal linear end-member mixtures of hyperspectral data. *Computers & Geosciences*, 2002, vol. 28, p. 809–817.

[41] BACHMANN, C. M., AINSWORTH, T. L., FUSIANA, R. A. Exploiting manifold geometry in hyperspectral imagery. *IEEE Trans. Geosci. Remote Sens.*, 2005, vol. 43, no. 3, p. 441-454.

[42] ADAMS, J. B., SMITH, M. O. Spectral mixture modeling: A new analysis of rock and soil types at the Viking Lander 1 suite. *Journal of Geophysical Research*, 1986, vol. 91, p. 8098-8112.

[43] BOARDMAN, J. W. Inversion of imaging spectrometry data using singular value decomposition. In *Proceedings of IEEE Symposium of Geoscience and Remote Sensing (IGARSS)*, 1989, p. 2069-2072.

[44] HEINZ, D., CHANG, C.-I. Fully constrained least squares linear spectral mixture analysis method for material quantification in hyperspectral imagery. *IEEE Trans. Geosci. Remote Sens.*, 2001, vol. 39, no. 3, p. 529–545.

[45] BROADWATER, J., CHELLAPPA, R. Hybrid detectors for subpixel targets. *IEEE Trans. on Pattern Analysis and Machine Intelligence*, 2007, vol. 29, no. 11, p. 1891–1903.

[46] RICHARDS, J. A., JIA, X. Using suitable neighbors to augment the training set in hyperspectral maximum likelihood classification. *IEEE Geosci. Remote Sens. Lett.*, Oct. 2008, vol. 5, no. 4, p. 774–777.

[47] RUMELHART, D. E., McCLELLAND, J. L. *Parallel Distributed Processing*. Cambridge, MA: MIT Press, Jul. 1987.

[48] HORNIK, K., STINCHCOMBE, M., WHITE, H. Multilayer feedforward networks are universal approximators. *Neural Networks*, 1989, vol. 2, no. 5, p. 359–366.

[49] IRIE, B., MIYAKE, S. Capabilities of three-layered perceptrons. In *Proceedings of the Int. Joint Conf. Neural Netw.*, 1988, vol. 3, p. 1641–1648.

[50] GREEN, R.O., EASTWOOD, M. L., SARTURE, C. M., CHRIEN, T. G., ARONSSON, M., CHIPPENDALE, B. J., FAUST, J. A., PAVRI, B. E., CHOVIT, C. J., SOLIS, M., OLAH, M. R., WILLIAMS, O. Imaging spectroscopy and the airborne visible/infrared imaging spectrometer (AVIRIS). *Remote Sens. Environ.*, 1998, vol. 65, pp. 227–248.

About Authors …

Fereidoun A. MIANJI received the M.S. degree in medical engineering from the Sharif University of Technology, Iran, in 1997. He is currently pursuing the Ph.D. degree in the Department of Information Engineering, School of Electronics and Information Technology, Harbin Institute of Technology, China. His research interests focus on digital image processing, hyperspectral image processing and application, and medical imaging.

Ye ZHANG received the M.S. and Ph.D. degrees in communication and information science from the Harbin Institute of Technology, Harbin, China, in 1985 and 1996, respectively. He is a Professor with the Department of Information Engineering, School of Electronics and Information Technology, Harbin Institute of Technology. His research interests include hyperspectral image processing and application, image and video compression, imaging scout, and vision matching. Dr. Zhang is a member of the Chinese Signal and System teaching committee and the Commission Science Technology and Industry for National Defense expert committee.

Asad BABAKHANI received the M.S. degree in medical engineering from the Sharif University of Technology, Iran, in 1997 and his Ph.D. degree in mechatronics from the Harbin Institute of Technology, Harbin, China in 2007. Dr. Babakhani is a member of national expert committee for standardization & industrial research. He is currently an Assistant Professor with the Gamma Irradiation Research Center, Iran. His research interests include image & data processing and robotics.